Wafer-Scale 1T′ MoTe₂ for Fast Response Self-Powered Wide-Range Photodetectors

Jiatong Mao, Youqi Zhang, Yinuo Zhang, Yunan Lin, Yao Feng, Yongqi Hu, Muhammad Shafa, and Yi Pan*

Cite This: *ACS Appl. Mater. Interfaces* 2023, 15, 28267−28276

Read Online

ACCESS | 📊 Metrics & More | 📖 Article Recommendations | 🆘 Supporting Information

ABSTRACT: The semimetal-based photodetector possesses the intrinsic advantage of high response speed, low power consumption, and wide-range photoresponse. Here, we report the synthesis and application of 1 inch wafer-scale polycrystalline few layer $1T'$-$MoTe_2$ on the SiO_2/Si substrate by employing a modified chemical vapor deposition method of predeposition of precursors. A continuous film with seamlessly stitched micrometer scale grains has been realized, and the pure $1T'$ phase was confirmed by Raman spectroscopy. An asymmetric metal electrode photodetector device of Pd-$MoTe_2$-Au was designed and fabricated by using shadow mask-assisted UHV deposition. By measuring the self-powered photocurrent under the illumination of Xe lamp, we show that the device is sensitive to a wide spectra range ($\lambda = 320-1200$ nm) while maintaining high performance of the ON/OFF ratio ($\sim 10^3$), responsivity (1.2 A/W), and specific detectivity (7.68×10^{12} Jones). Under 450, 648, and 850 nm pulsed laser illumination, the response time achieves tens of microsecond scale. The device shows polarized photoresponse as well. Our work may promote the potential application of a self-powered high-performance photodetector based on $1T'$-$MoTe_2$.

KEYWORDS: $1T'$ $MoTe_2$, topological semimetal, chemical vapor deposition, wide-range photodetector, self-powered
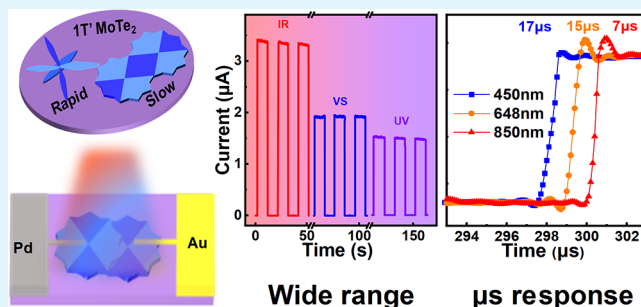
INTRODUCTION

The layered 2D materials hold great promise for a high-performance photodetector (PD) that could be used in wearable devices, due to the intrinsic advantage of mechanical flexibility, high response rate, and wide detection range of spectra.[1−5] The semimetallic $1T'$ $MoTe_2$, as a member of layered 2D transition metal dichalcogenides (TMDCs), thus becomes an emerging candidate for such high-performance PDs. The bulk $MoTe_2$ could condense in the hexagonal 2H phase or monoclinic $1T'$ phase at room temperature. The trigonal prismatically coordinated 2H-$MoTe_2$ is a semiconductor, while the distorted octahedral coordinated $1T'$ $MoTe_2$ is a semimetal.[6,7] At low temperatures, the $1T'$ phase transforms into the orthorhombic T_d phase, which is topological Weyl semimetal due to the broken spatial inversion symmetry.[6] The rich phase diagram renders $MoTe_2$ an attractive material for fundamental research and device application. In the past few years, the synthesis and phase engineering of large-scale $MoTe_2$ films has been intensively explored.[8−14] Meanwhile, superior performance of semi-metallic TMDC-based PDs is emerging, e.g., the anisotropic photoresponse of WTe_2, robust edge photocurrent response of $MoTe_2$, and polarized infrared response of $MoTe_2$ hetero-structures.[15−17] It was also reported recently that both $1T'$ and

T_d-$MoTe_2$ show ultra-fast photoresponse, while the photo-carrier lifetime is higher in the $1T'$ phase.[18]

On the other hand, the application of PD in portable devices requires a balance between high performance and low power consumption. Thus, the self-powered PD that could convert the optical signal into an electrical signal without external power becomes a good choice. For the 2D semimetals, e.g., graphene, it could function as a self-power PD as long as the photocarriers are effectively separated by a built-in field and accumulated to a reasonably high external current. This can be achieved by an internal electric field arising from the Schottky barrier between 2D materials and the metal electrode.[1,3]

Although the 2D semimetals show lots of advantages, the exploration of 2D semimetal-based PD largely focuses on graphene so far. Similar to graphene, the $1T'$-$MoTe_2$-based photodetector possesses the intrinsic advantage of high response speed, low power consumption, and wide wavelength range, owing to their unique band overlap structure.[4]
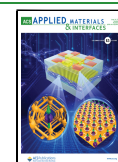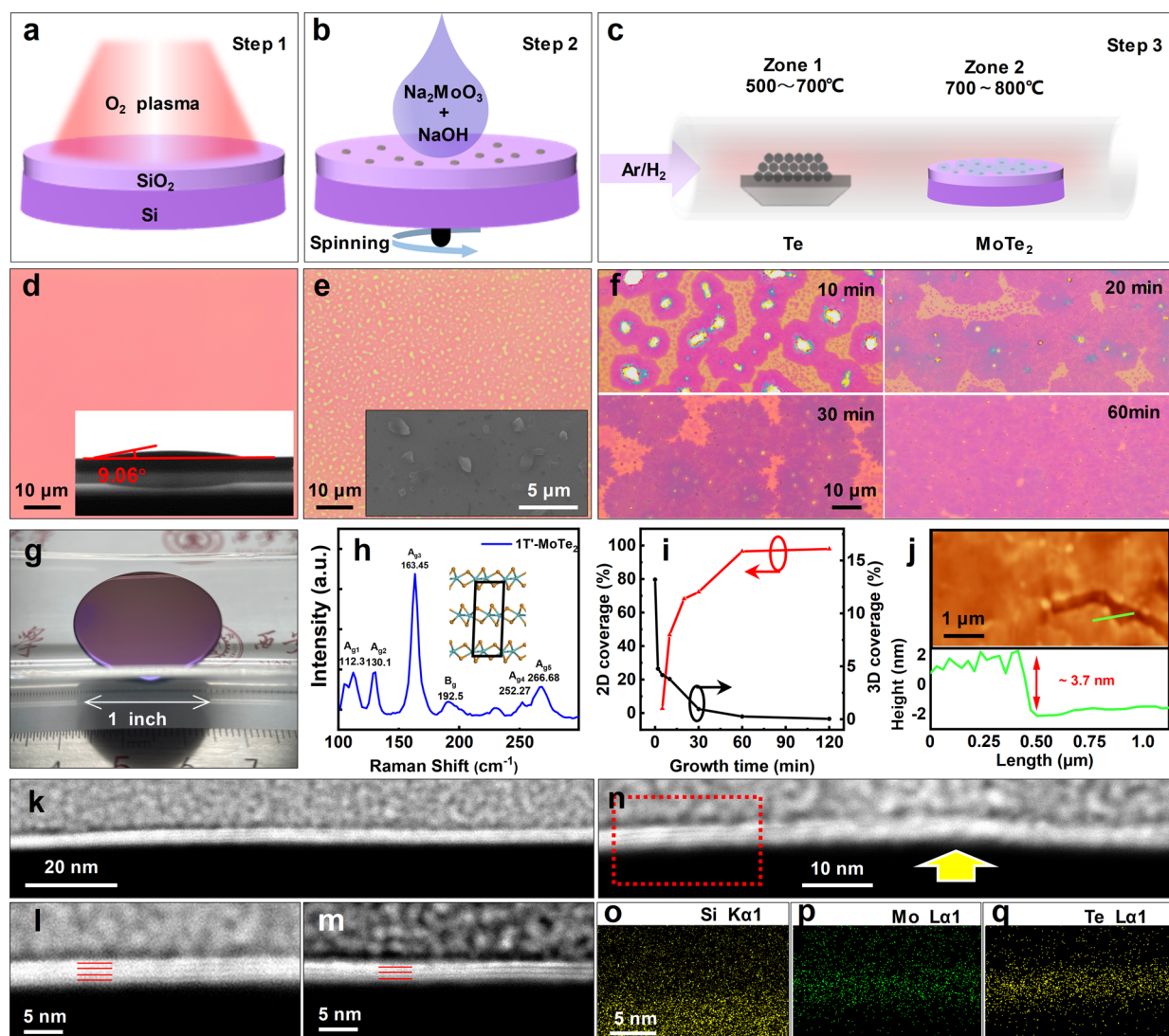
Figure 1. Synthesis strategy and characterization of the wafer-scale continuous 1T′-MoTe$_2$. (a−c) Schematic diagram of the growth steps: (a) Step 1: oxygen plasma etching of SiO$_2$/Si substrate; (b) Step 2: spin coating of precursor solution; (c) Step 3: tellurization at high temperature in a hot wall tube furnace. (d−f) OM images of SiO$_2$/Si substrate surface after each step. (d) Clean hydrophilic surface due to oxygen plasma treatment. Inset: contact angle of DI water droplet. (e) Surface with precursor clusters. Inset: SEM image showing the clusters; (f) Series of images showing the evolution of MoTe$_2$ films of 10, 20, 30, and 60 min growth time. (g) Picture of the 1 inch SiO$_2$/Si wafer substrate with a hydrophilic surface. (h) Raman spectra of MoTe$_2$ showing peaks corresponding to 1T′ phase. Inset: side view atomic structure model of the monoclinic 1T′-MoTe$_2$. (i) Plot of the projection coverage of 2D film (black curve) and 3D clusters (red curve) areas as a function of growth time. (j) AFM image of 1T′-MoTe$_2$ surface and the height profile along the green line over a step edge. (k−m) Cross-sectional HAADF-TEM images obtained from a continuous 1T′ MoTe$_2$ film. (k) Overview image was taken within a single grain. (l, m) Zoom-in images reveal the thickness of 4 and 3 monolayers of two samples. (n) Zoom-in image of a grain boundary within the continuous film, as indicated by the yellow arrow. (o−q) EDS elemental mapping of (o) Si, (p) Mo, and (q) Te distribution in the area enclosed by the red rectangular in (n).

Specifically, the short transient lifetime of photoexcited carriers permits ultra-fast response; the absence of band gap enables the wide range of detectable photon energy from zero to a few eV, i.e., from far IR to UV in the spectra.[1,2,19] However, the investigation on 1T′-MoTe$_2$-based self-powered high-performance PD is still lacking so far. It is mainly hindered by the availability of wafer-scale continuous samples optimized for PD devices. Additionally, the 1T′-MoTe$_2$ device requires a tailored design and fabrication process to maximize the crucial parameters of merit.

In this work, we synthesized 1 inch wafer-scale polycrystalline few layer 1T′-MoTe$_2$ on the SiO$_2$/Si substrate by employing the modified chemical vapor deposition (CVD) method of predeposition of precursors. The micrometer scale grains of pure 1T′ phase were revealed by the polarized optical microscope and Raman spectroscopy. Asymmetric structure PD devices with Pd/Au electrodes were designed and fabricated utilizing the shadow mask-assisted UHV deposition technique. By measuring the self-powered photocurrent under the illumination of an Xe lamp, we show that the device is sensitive to a wide spectra range (λ = 320−1200 nm) while maintaining a high performance of ON/OFF ratio (5×10^3), responsivity (1.2 A/W), and specific detectivity (7.68×10^{12} Jones). Under 850 nm laser, the response time achieves the microsecond scale. The device shows polarized photoresponse as well. Our work promotes the potential application of self-powered high-performance PD based on 1T′-MoTe$_2$.
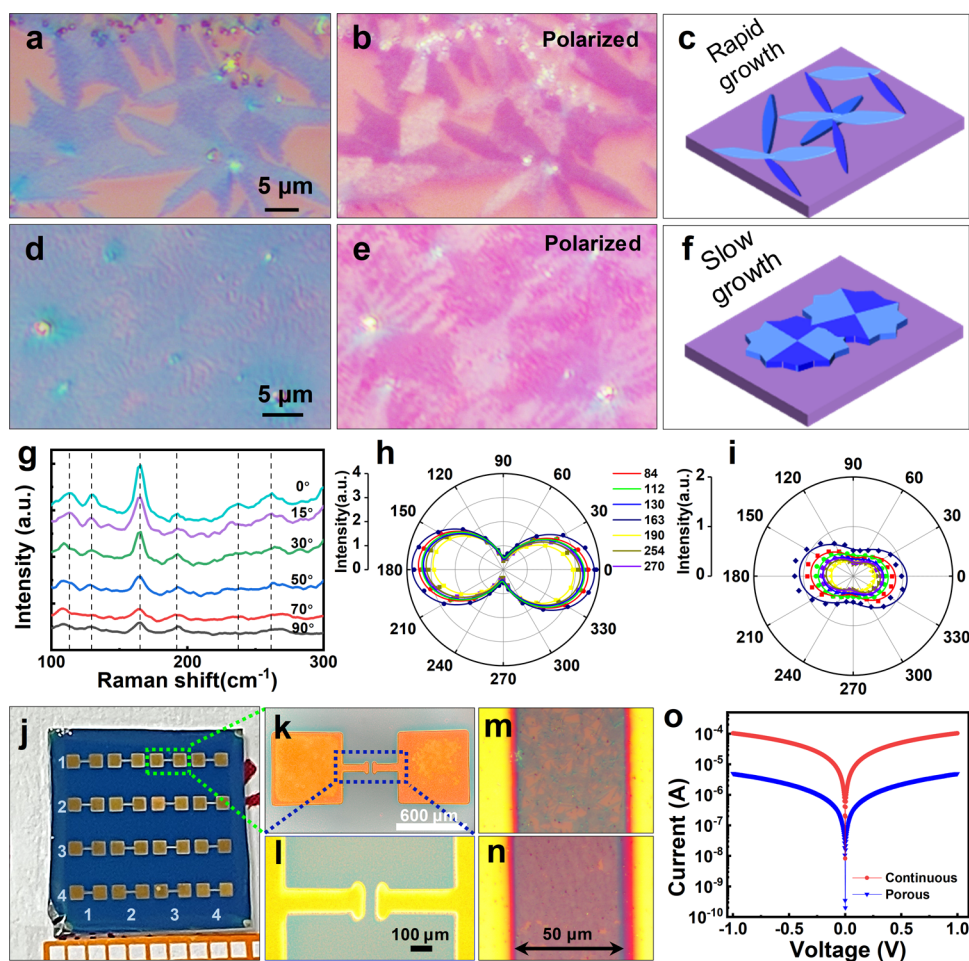
Figure 2. Grain structure analysis and transport property optimization of the 1T′-MoTe$_2$ film. (a) OM image and (b) POM image of the porous film composed of loosely connected highly crystallized islands, which was formed in the rapid growth mode under the Te-rich condition as schematically illustrated in (c). (d) OM image and (e) POM image of the continuous film composed of seamlessly stitched microdomains as schematically illustrated in (f), which was formed in the slow growth mode under the Te-deficiency condition. (g) ARPRS of porous 1T′-MoTe$_2$ dependent on the polarized angle from 0° to 90°. (h, i) Polar plots of Raman intensity of indicated Raman modes as a function of polarization angle taken on (h) porous and (i) continuous film. (j) The photo of a 4 × 4 array of two terminal devices fabricated on the large-size film samples. (k) OM image of a single device. (l) Zoom-in OM image of the channel region. Contrast enhanced zoomed-in image showing the continuous film (m) and porous film (n) between two neighboring electrodes. (o) Typical I−V curve obtained from the device fabricated on continuous (red) and porous (blue) films.

◼ RESULTS AND DISCUSSION

Growth of Wafer-Scale Continuous 1T′-MoTe$_2$. The large-scale continuous 1T′-MoTe$_2$ films were synthesized on 1 inch wafers and similar size SiO$_2$/Si substrates utilizing the CVD method in a dual heating zone hot wall tube furnace. The three main steps are demonstrated in Figure 1a−c. Briefly, the substrate was first pretreated by oxygen plasma etching, then spin-coated with a water solution of Na$_2$MoO$_3$ as a Mo precursor, followed by chemical reaction with Te vapor in the furnace and naturally cooled down at last. Under optimized conditions, the wafer-scale 1T′-MoTe$_2$ films of desired morphology and thickness could be produced with good repeatability. More details of growth parameters can be found in the method section. The oxygen plasma etching procedure could thoroughly clean the surface, as shown in the flawless image in Figure 1d and the photograph of a whole 1 inch wafer in Figure 1g. More importantly, it dramatically improves the hydrophilicity of the surface. The contact angle of the (deionized) DI water droplet is 71.8° before the treatment, as shown in Figure S1. In contrast, it could be reduced to 9°

(inserted in Figure 1d), which proved the effect of oxygen plasma treatment. On such a hydrophilic surface, the spin-coating of the dilute solution resulted in a continuous thin wetting layer. After drying up, it transformed into homogenously distributed precursor clusters, as shown in the optical microscope (OM). The scanning electron microscope (SEM) image inserted in Figure 1e reveals that the diameter of the clusters is a few micrometers. The density of the precursor could be precisely tuned by adjusting the concentration of the solution. Energy dispersive spectrometer (EDS) analysis shows that the element in the cluster is mainly Mo and Na (Figure S2), confirming the successful deposition of the precursor. NaOH is an essential promoter for 2D growth since the Na$^+$ ions could reduce the growth temperate and the OH$^−$ suppresses the vertical growth.[12]

In the following high-temperature tellurization reaction, the 2D MoTe$_2$ islands nucleated at each precursor cluster and grew around it, while the clusters were shrinking and flattening, as displayed in the series of images in Figure 1f. For the growth time of ∼60 min, the expanding islands were eventually

merged into a continuous film with coverage above 98%, as shown in the zoom-in OM image in Figure 1f. We have found two key factors that determine the uniformity of the sample. The first is the precursor particle size and density. If the precursor particle diameter is below ten micrometers and homogeneously distributed on the substrate, the 3D feature would disappear and a seamless film could be formed. Oxygen plasma pretreatment of the substrate is thus crucial for controlling the precursor size and density. The second is the small amount of H_2 in the carrier gas, which could reduce the oxides and etch away the extra 3D features, most likely because the 2D vdW surface is more inert compared with the 3D structure with dangling bonds. Under optimized conditions, the 3D precursor particles could completely transform to 2D, as demonstrated in the zoomed-in OM and SEM images in Figure S3. We also observe that when the Te powder was heated to a higher temperature, the film grew faster and the $MoTe_2$ grain shows more regular edges. However, it ended up with a porous film with coverage below 70%, as shown in Figure S4. Under an optimized condition, the statistical analysis of 2D film coverage and average cluster size versus growth time is plotted in Figure 1i. The curves indicate that the disappearance of clusters is synchronizing with the full coverage. It implies that the deposited precursor clusters could provide adequate Mo for a continuous film, and the 3D to 2D transformation is complete.

To further inspect the phase of the $MoTe_2$ film, Raman spectroscopy with a 532 nm excitation laser was employed. A typical Raman spectrum shown in Figure 1h reveals 6 evident peaks of the $MoTe_2$ specimen, as indicated by the red arrows (A_{g1}: 115 cm^{-1}; A_{g2}: 130 cm^{-1}; A_{g3}: 163 cm^{-1}; B_g: 192 cm^{-1}; A_{g4}: 252 cm^{-1}; A_{g5}: 270 cm^{-1}). These peaks nicely match the Raman mode of $1T'$-$MoTe_2$.[20] The sharpness of peaks proved that the sample is highly crystallized. We attribute the extra peak at 228 cm^{-1} to the substrate, since it also appears on the bear SiO_2/Si substrate (Figure S5). Interestingly, we did not observe any signal of 2H phase $MoTe_2$.

The microscopic surface morphology, the interface between the substrates and the thickness of the film has been characterized by the atomic force microscope (AFM) and transmission electron microscope (TEM). As shown in Figure 1j, the topographic AFM image demonstrates that the sample surface is atomically flat, while the height profile across a slit between the grains reveals the thickness of the film is about 3.7 nm, equivalent to 5 monolayers. In some other areas of the sample, we also observed a layer thickness of 4−6 nm. Although the thickness may fluctuate slightly, the sample surface is atomically flat within the same grain. As shown in Figure 1k, the overview of cross-sectional HAADF-TEM images taken within a single grain of a continuous $1T'$ $MoTe_2$ film sample shows the film is thin and uniform. In the zoom-in images (see Figure 1l,m), the 4 and 3 monolayer thickness could be directly resolved, which agrees well with the AFM results. The zoom-in TEM image in Figure 1n shows a grain boundary, as marked by the yellow arrow pointing to a small bump between two flat areas. It may suggest that the grains are well-stitched within the continuous film. The EDS elemental mappings of Si, Mo, and Te distribution within the red rectangular are shown in Figure 1o−q, which directly proved that our film is pure $MoTe_2$. The $MoTe_2$−SiO_2 interface is perfectly sharp and clean. Based on the systematic morphology and Raman spectra analysis, it is unambiguous

that the samples are highly crystallized polycrystalline few-layer $1T'$ phase $MoTe_2$ on the SiO_2 substrate.

Sample Optimization for Photodetector Devices. We then investigated the grain structure of the polycrystalline film and its influence on electron transport performance. Since the $1T'$-$MoTe_2$ is a monoclinic biaxial crystal, it shows anisotropic adsorption and pleochroic reflection of light.[21] For the polarized incident light, each single crystalline grain in the film shows orientation-dependent brightness, thus the polarized optical microscope (POM) is suitable for grain structure characterization. The OM and POM images of the same area in a porous film sample are shown in Figure 2a,b, respectively. It clearly reveals that the film is composed of micrometer-scale single crystal grains with straight edges and clear boundaries, as demonstrated schematically in Figure 2c. However, there are empty spaces between the grains, thus giving rise to the porous morphology. On the other hand, the OM and POM images of the continuous film in Figure 2d,e reveal that it is composed of small grains with irregular boundaries, as demonstrated in Figure 2f. Although the grains are smaller, the whole film does not contain many empty areas. The normal Raman spectroscopy of the two types of samples did not show much difference. However, the angle resolution polarized Raman spectra (ARPRS) could tell some details about the crystallinity of the two. As shown in Figure 2g, the obvious polarization angle-dependent Raman intensity of porous $1T'$-$MoTe_2$ confirmed that the grains are highly crystalized and the grain size is comparable to the laser beam spot in the micrometer scale. Additionally, the polar plots of Raman intensity (see Figure 2h,i) show that the anisotropy in the continuous film is weaker than the porous film, suggesting the grains in the continuous film is smaller and more randomly oriented, which agrees well with the POM observation.

We attribute the reason for the two distinct morphologies of $1T'$ phase $MoTe_2$ to the growth dynamics parameters. The porous sample was formed in a rapid growth mode with a high carrier gas flow of 70−100 sccm Ar/H_2 (90:10%). Under such Te-rich conditions, the anisotropic growth along the [010] direction is dominating, thus the radially distributed ribbon shape grains are formed, which is consistent with the literature.[22] Note that the large-scale $1T'$-$MoTe_2$ synthesized by the traditional CVD method is in the porous structure.[22,23] The continuous film was realized in a slow growth mode with optimized parameters, i.e., reducing the Te constriction by lowering carrier gas flow rate of 10−25 sccm Ar/H_2 (90:10%). Under such relatively Te-deficiency conditions, the anisotropic growth is suppressed, thus disk-like isotropic islands are formed, which seamlessly merged eventually. These films with tunable morphology could be test samples for transport measurement to optimize the photodetector devices.

To evaluate the basic transport properties of the films, a 4 × 4 array of two terminal devices (see Figure 2j) were fabricated by deposition of Au electrodes on the 10 × 10 mm^2 film samples using the shadow mask-assisted UHV PVD method. The OM image of a single device and the zoom-in OM image of the channel region are displayed in Figure 2k,l, respectively. The zoomed-in OM images in Figure 2m,n display the distinct morphology of the porous and continuous films between the metal electrodes. The domain structures could be observed in the POM images (Figure S6), where the continuous film shows much better quality. The I−V curves under the dark condition obtained on the devices are plotted in Figure 2o, and more I−V curves are shown in Figure S9. It reveals a typical ohmic

transport behavior of the metallic material, with the symmetric current for positive and negative bias. The resistance of the continuous film is dramatically lower and the current is more stable at low bias, demonstrating better quality compared with porous films. It implies that the seamless stitching grain boundary is indeed helpful for reducing charge carrier scattering. Such an effect has been intensively investigated in the polycrystalline graphene and applied in the corresponding devices.[24,25] The continuous 1T′-MoTe₂ film thus provides us the optimized sample for our photodetector devices.

The uniformity of the sample over the whole wafer is important for its application as a PD device. We have evaluated our sample in three aspects that affect the device's performance. First, the uniformity of the phase was checked by taking Raman spectra at random locations on the sample, which confirmed that the film is pure 1T′ phase MoTe₂, as shown in Figure S7. Second, the uniformity of flatness in the sense of 3D/2D ratio was checked at different locations on the sample by taking high-magnification OM images, which reveal that the 3D particles have been completely transformed into the 2D film, as shown in Figure S8. Third, the uniformity of basic electric transport property was evaluated by measuring the $I-V$ curves of multiple devices in an array fabricated on the wafer size film, which reveals that the $I-V$ curves obtained from different devices are nicely consistent with each other, as plotted in Figure S9. These results have proved that the uniformity of the sample could fulfill the requirement of the photodetector devices.

PD Devices: Self-Powered, Wide-Range, and Fast Response. We then designed and fabricated the PD devices based on the continuous 1T′-MoTe₂ film. As shown in Figure 3a, it is in an asymmetric metal electrode structure of Pd-MoTe₂-Au. The devices were fabricated by directly depositing patterned metal electrodes with shadow masks under the UHV condition. Here, we chose Pd and Au as electrodes since the work function (WF) of 1T′-MoTe₂ (~5.15 eV)[26] falls in between that of Pd (~5.4 eV) and Au (~5.1 eV). When the Pd (Au) electrode is in contact with 1T′-MoTe₂, the contact potential gives rise to slight charge (hole) doping to the 2D semimetal 1T′-MoTe₂, as shown in the schematic band diagram in Figure 3b. Thus, a lateral built-in electric field is formed within the 1T′-MoTe₂, the same as in the asymmetric electrode graphene PD device.[1] Thanks to the built-in field, the photocarrier can be effectively separated without external bias, which means that the PD could be self-powered. The unique band overlap of semimetal allows the adsorption of photons of varying energies, endowing the PD with wide-range photoresponse in the light spectra.

To investigate the performance of the device, we measured the photocurrent in a dark chamber equipped with a high-pressure Xe lamp (λ = 300−1200 nm), mechanical shutter (>1 ms), and band-pass filter. The black curve in Figure 3d is the dark current, which typically shows nano ampere-level current at zero bias. The green curve displays the photocurrent under white light illumination in the bias range from −1.0 to 1.0 V. The minimum in the green curve shifted from zero to about 0.1 V, confirming that the asymmetric design of the device has excellent photo response. The zero bias photocurrent could reach 7.6 μA, giving rise to a high ON/OFF ratio of ~10³. To demonstrate details of the open-circuit voltage (OCV) and short-circuit current (SCC), the photocurrent curves under different illumination power are plotted in Figure 3d. It shows that the OCV and SCC increase with the illumination intensity
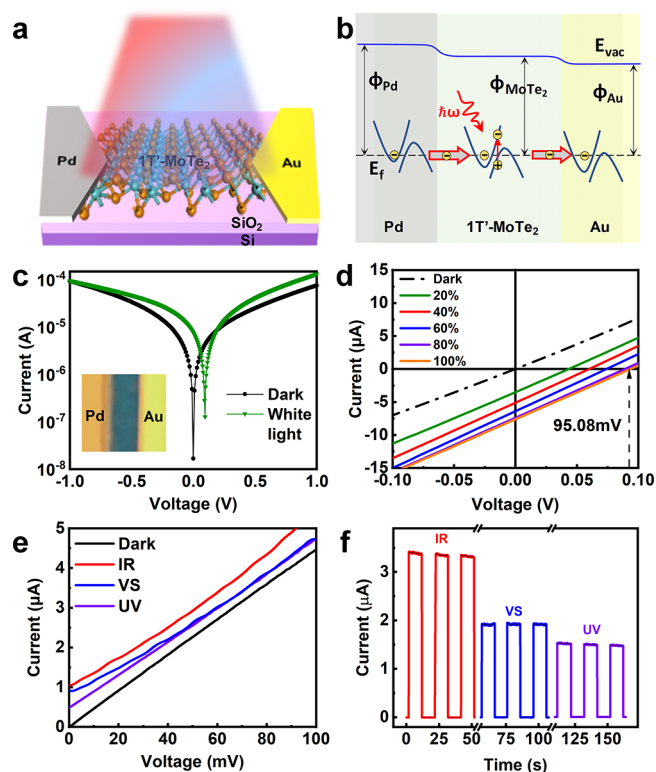

Figure 3. Configuration and performance of 1T′-MoTe₂ PD device with the asymmetric metal electrodes of Pd and Au. (a) Schematic view of the PD device. (b) Illustration of the mechanism of the PD. Photocarriers are generated in the semimetal with band overlap by adsorption of photons with various energy, and separated by the built-in electric field arising from Pd-MoTe₂ and MoTe₂-Au contact potential. (c) Logarithmic plot of $I-V$ curves under illumination of full spectra of Xe lamp (green) and under the dark condition (black). Inset: zoom-in OM image showing the Pd-MoTe₂-Au asymmetric structure. (d) $I-V$ curves obtained with varying light power intensity. (e) $I-V$ curves obtained in the dark and under the illumination of constant light power intensity with bandpass filters for IR (red), visible (blue), and UV (purple) light. (f) Self-powered (zero bias) $I-t$ curves obtained under shutter-controlled pulse illumination of IR, visible and UV light with the same power intensity.

until saturates eventually. The OCV and SCC reach a maximum value of 95.08 mV and 7.6 μA, respectively. These results demonstrate that our UHV-fabricated Pd-1T′-MoTe₂-Au PD device could effectively separate the photocarrier and suppress the recombination. The performance is comparable to the recent work on ReSe₂ with sophisticated transferred metal integration electrodes.[27,28]

We then insert the band-pass filters (UV 350−400 nm, VS 450−850 nm, IR 850−1100 nm) into the beam path to check the photocurrent response to different wavelengths. As shown in Figure 3e, the red, blue, and purple curves are the photocurrent obtained with UV, VS, and IR filters, respectively. The black and green curves display the photocurrent under white light and dark conditions. It reveals that the PD device is sensitive to all of the wavelength ranges separated by the filters. Although the UV response is a little weaker than IR and VS, it still creates μA-level short-circuit current, which is reasonably high for UV detection. Figure 3f shows the zero-bias $I-t$ curves of the PD device under pulsed illumination (created by a mechanical shutter) in different wavelength range. It demonstrates that the device can generate
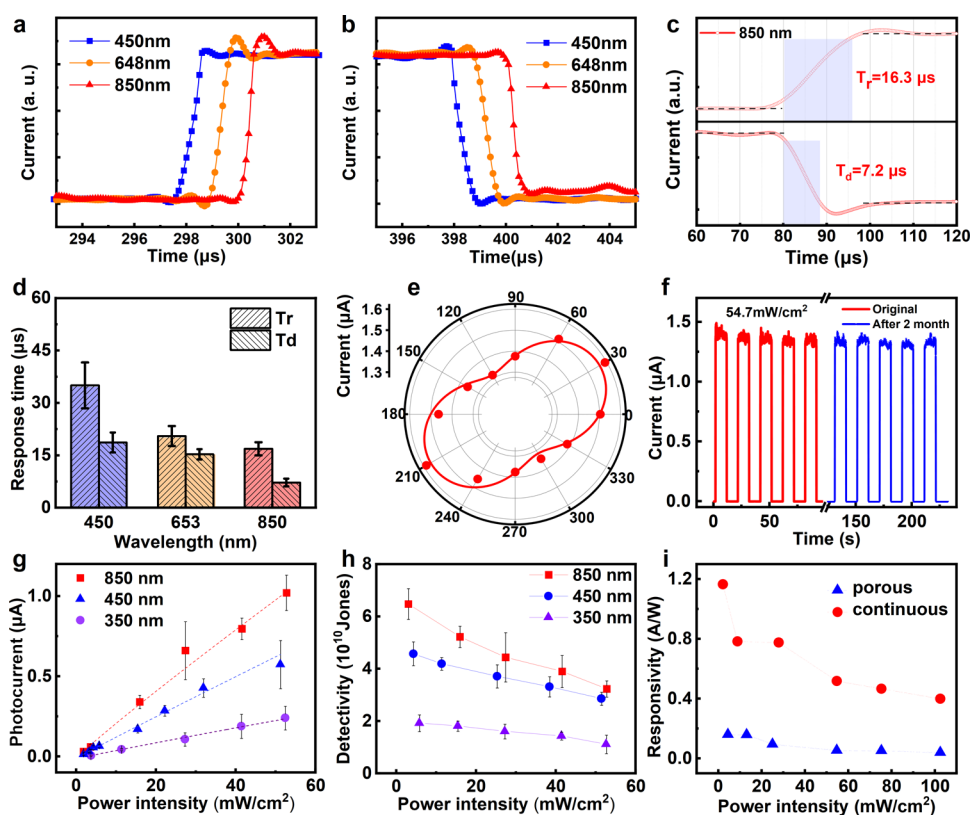
Figure 4. Response time, photoresponsivity, and detectivity of the self-powered 1T′-MoTe$_2$ PD. (a, b) Rising and decaying edges of the output photocurrent pulses respond to 450 (blue), 648 (orange), and 850 nm (red) pulsed laser illumination. (c) High-resolution measurement of photoresponse to 850 nm laser to determine the rising and decaying time. (d) Statistical results of rising and decaying time responding to the pulsed laser of various wavelengths. (e) Anisotropic response for the linear polarized light of Xe lamp. The ratio of anisotropy ellipse is 1.2. (f) I−t curves of the PD device under 54.7 mW/cm^2 illumination of Xe lamp. Red: fresh device; blue: after 2 months. (g, h) Photocurrent and specific detectivity of the PD devices as a function of incident power density, for the light of various wavelengths. (i) Comparison of the photoresponsivity devices of the same dimension fabricated on continuous (red) and porous (blue) films, under 850 nm laser illumination.
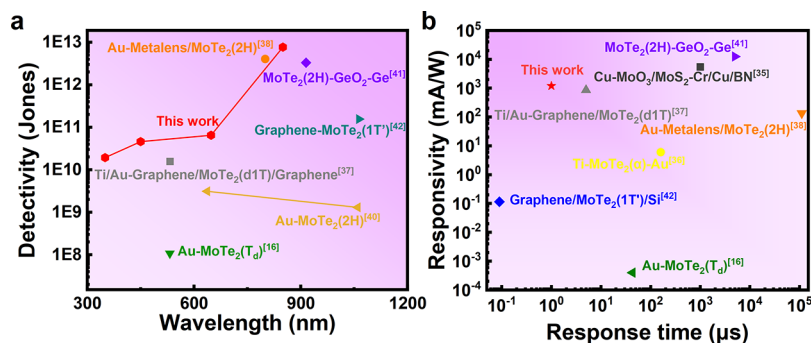

Figure 5. Comparison of the key parameters of MoTe$_2$-based PD. (a) Specific detectivity of the devices at varying wavelengths. (b) Responsivity of the devices versus the response time.

very sharp current pulses, with SCC values of 3.386, 1.913, and 1.498 μA for the bandpass IR, VS, and UV illumination, respectively. The photocurrent measurement confirms that the Pd-1T′-MoTe$_2$-Au PD device is sensitive to a wide range of wavelength, herein from 320 to 1200 nm due to the limitation of our light source. In principle, the semimetal-based PD does not have a minimum detective limit of photon energy due to the zero-gap band structure,[29] contrary to the semiconductor-based PD which is limited to the photon energy above the band gap.[30] Thus, our PD may work in the wavelength range beyond 320−1200 nm, as is already reported in the same

material.[22] Further study on the sensitivity of such PD to DUV and THz light is required in the future.

In order to examine the response speed of the PD device, we switched the light source to fiber laser (λ = 850, 648, and 450 nm), which could generate square-wave-like light pulses with much sharper edges than the shutter. To precisely evaluate the rising and decaying time of the photoresponse signal, the photocurrent was converted to voltage by using a transimpedance amplifier, and then captured by a digital storage oscilloscope (Figure S10). The photocurrent under 850, 648, and 450 nm pulsed laser display square wave-type signal with flat top and sharp edges, as shown in Figure 4a,b. The zoomed-

in high-resolution curves at rising and decaying edges of a single pulse under 850 nm laser illumination are displayed in Figure 4c. The shadow regions indicate the 10 and 90% position of rising or decaying edges, thus we can obtain the rising time (T_r) as 16.3 μs and the decaying time (T_d) as 7.2 μs, for this particular pulse. The statistical analysis results of T_r and T_d for various wavelengths are demonstrated in Figure 4d. It shows that the response time of our devices is below 50 μs for all measured wavelengths. To our knowledge, this is among the best results for 1T′-MoTe$_2$ PD so far, as compared with the literature in Figure 5. Note that the square pulse generated by our fiber laser is not an ideal square wave, which have response time of a few microseconds, as calibrated with a submicrosecond-level response silicon PIN PD. Our photoresponse signal did not show obvious lagging compared with the light signal. Thus, we anticipate the response limit of our Pd-1T′-MoTe$_2$-Au device might be lower.

As already shown in Figure 2, our sample has anisotropic reflection to polarized light due to the adsorption being orientation dependent on the single crystal grain. To test the polarized photoresponse, we modified our Xe lamp source by adding a polarizer in the beam path and then performed the orientation-dependent photoresponse measurement by varying the polarizer angle. As plotted in the polar axis in Figure 4d, the photocurrent is indeed showing a dominant orientation in 30/210°. The red curse is fitted according the equation:[31]

$$I_{ph}(\theta) = I_{pmax} \cos^2(\theta) + I_{pmin} \sin^2(\theta) \tag{1}$$

where θ is polarization angle. The I_{pmax}/I_{pmin} ratio 1.2 can be deduced from the curve, which implies that our PD device has potential application in polarized light detections.

Additionally, the duration of our PD was evaluated by comparing the photoresponse of the same device after ambient condition storage for 2 months, as shown in Figure 4f. It clearly shows that both I_p and response speed are perfectly maintained, indicating that it is highly stable in air.

Figure 4g shows the linear fitting of I_p versus light intensity for various wavelengths, according to the equation $I_p = cP^\alpha$, where c is a constant, and α is the exponent index to fit.[32] The fitting indicates linear relation for all the wavelengths, and index α is 0.97, 0.95, and 0.91 for 850 (laser), 648 (laser), and 350 nm (LED), implying effective suppression of electrons and holes recombination. Based on the systematically acquired experimental results, we calculated the key parameters of merit for our PD device, i.e., responsivity (R) and specific detectivity (D^*). The responsivity R represents the capability of converting light energy to electronic signal. It was calculated according to the equation:

$$R = \frac{I_p}{AP} \tag{2}$$

where I_p is acquired by subtracting dark current I_{dark} from photocurrent I_{light}. P is the power intensity of incident illumination, while A is the effective illumination area of the device. D^* was calculated according to the equation:[33]

$$D^* = \frac{RS^{1/2}}{(2eI_{Dark})^{1/2}} \tag{3}$$

The calculated specific detectivity and responsivity values of power intensity is shown in Figures 4h and S11. For 850, 648, and 350 nm illumination, the best responsivity values we obtained are 1046, 676.7, and 330.8 mA/W, while the best

detectivity values are 6.48×10^{10}, 4.57×10^{10}, 1.92×10^{10} Jones, respectively. Such performance is among the top tier of 2D semimetals. Also, the performance for IR is the highest, followed by VS and UV. For the broadband illumination, the responsivity and specific detectivity reach 1193 mA/W and 7.68×10^{12} Jones (see Figure 4i). We also compared the performance of the PDs fabricated on the porous film, as displayed by the blue dots in Figure 4i, which shows measurable responsivity but at least one order of magnitude lower than the PDs on the continuous film.

In Figure 5 and Table S1, we summarized the key parameters of our device and other MoTe$_2$-based PD from the literature.[16,22,34−42] It shows that the ON/OFF ratio, specific detectivity, and response speed of the Pd-1T′-MoTe$_2$-Au device is among the best. It is sensitive to a rather wide range in the light spectrum, with the best detectivity in near-infrared, as shown in Figure 5a. The responsivity of our device is in the top tier, but a little lower than ref 36, 41. This is mainly because our device is working at zero bias, thus the charge separation is not as efficient as those with an external electrical field. However, our device and is work in self-powered mode with a very fast response, which is advantageous for low power consumption. Since it is much easier to fabricate integrated circuits on the wafer-scale film, we anticipate it may find application in the next generation of photodetectors with high performance and low energy consumption.

CONCLUSIONS

In conclusion, we have synthesized wafer-scale continuous polycrystalline 1T′-MoTe$_2$ films by a renovated immobile precursor CVD method, and then investigated the asymmetric metal electrode PD based on the semimetal 1T′-MoTe$_2$ materials. The film is in pure 1T′ phase, with the grain size of a few micrometers and thickness of 3−6 monolayers. The continuity and coverage could be improved by tuning the dynamic parameters and thus enhancing the transport property for the application of PD. The PD is sensitive to a wide spectra range (λ = 320−1200 nm) while working in self-powered mode. Under the illumination of white light, the ON/OFF ratio reaches 5×10^3, while R and D^* could reach 1.2 A/W and 7.68×10^{12} Jones, respectively. Under 850 nm laser, the response time is in the microsecond scale (T_r 16 μs, T_d 7.2 μs). It also shows polar response with the I_{pmax}/I_{pmin} ratio of 1.2. These results shed light on the application of large-scale 1T′-MoTe$_2$ in high-performance photodetector in the future.

EXPERIMENTAL SECTION

Sample Growth. The wafer-scale 1T′-MoTe$_2$ samples were synthesized utilizing the CVD method. The single-side polished SiO$_2$ (300 nm)/Si wafers were used as the substrates, which were either whole 1 inch wafers or 10 mm × 10 mm squares cut from 4 inch wafer (p(100), Yuanjing Electronic Technology Co., Ltd). First, the ultrasonically washed substrate (in the sequence of acetone, isopropanol, ethanol, and deionized water) was (etched) by Oxygen plasma (PT-5ST, SANHOPTT) for 20 min with 35 W RF power to enhance the surface hydrophilicity. Then, the liquid precursor solution (50 mg of sodium molybdate and 50 mg of sodium hydroxide dissolving in 5 mL DI water) was spin-coated on the pretreated substrate at 8000 rpm for 60 s. Afterward, the quartz boat containing the naturally dried substrate and another boat with 80 mg of Te powder (Alfa Aesar, 99.999%) were placed in the two heating zones of the tube furnace (CNF-3Z, BEQ), respectively. The sealed tube was pumped down to 1−2 Pa, slowly vented with 200 sccm Ar/

H_2 (90:10%) mixture gas to ambient pressure, and kept for 10 min. Then, the gas flow rate was reduced to 10 sccm and maintained at that value, while the temperature of both heating zones was ramped up to 700 °C and kept for 30 min. At last, the furnace was naturally cooled down to room temperature.

Sample Characterization. The sample morphology was characterized using an optical microscope with polarizer filter M330-3M180, AOSVI) and an atomic force microscope (Cipher S AFM, OXFORD INSTRUMENTS). The contact angle of the precursor solution droplet on the substrate was measured with a contact angle meter (OCA25, Dataphysics). The surface structure measurements were carried out with a scanning electron microscope (MIRA3-LMH, Tyco Electronics) at 15 kV. The interface structure and elemental mapping analysis were carried out with TEM (JEM-ARM200F). The Raman spectra were carried out with a confocal Raman spectrometer (HORIBA) with a 532 nm laser as excitation. The electric transport properties were measured with a dual-channel source meter (Keithley 2636B).

Device Fabrication. The devices were fabricated within a home-built UHV multisource physical vapor deposition system under the pressure lower than 10^{-5} Pa. The Cr, Pd, and Au electrodes of 10−100 nm were directly deposited on the sample surface, while the designed patterns were realized by using custom-made metal shadow masks, and thickness calibrated by using QMS (TMC13, PREAVC).

Photoresponse Measurement. All the measurements were carried out at room temperature and under the ambient air condition. A high-pressure Xe lamp (CME-SL300, Microenerg) equipped with grating polarizers (HCN12-D25 JIANGYIN) was utilized as polarized and nonpolarized light source with continuous spectra (wavelength 300−2500 nm). A manual rotation stage was used to rotate the polarizer for the linear polarization-dependent response measurements. The pulsed laser beams were provided by fiber lasers (Oaebt OF-20B, λ = 420, 648, and 850 nm) with a PWM light-dimming controller. The fast response of the device was measured with a home-built system with a transimpedance amplifier and digital storage oscilloscope (DSO-X3052A, Agilent).

ASSOCIATED CONTENT

Supporting Information

The Supporting Information is available free of charge at https://pubs.acs.org/doi/10.1021/acsami.3c05902.

Contact angle of DI water droplet SiO_2/Si substrate surface without plasma etching; SEM and EDS images of a precursor cluster; OM and SEM images of the continuous film; OM images of the porous film; Raman image of SiO_2/Si substrate; POM image of the continuous film and porous film; Raman spectra, OM images at random locations on a continuous film; 2 terminal device array; schematic structure of the home-built optoelectronic measurement system; calculated responsivity versus power intensity; comparison of the key parameters of $MoTe_2$-based PD (PDF)

AUTHOR INFORMATION

Corresponding Author

Yi Pan − Center for Spintronics and Quantum Systems, State Key Laboratory for Mechanical Behavior of Materials, Xi'an Jiaotong University, Xi'an 710049, China; orcid.org/0000-0003-1978-475X; Email: yi.pan@xjtu.edu.cn

Authors

Jiatong Mao − Center for Spintronics and Quantum Systems, State Key Laboratory for Mechanical Behavior of Materials, Xi'an Jiaotong University, Xi'an 710049, China

Youqi Zhang − Center for Spintronics and Quantum Systems, State Key Laboratory for Mechanical Behavior of Materials, Xi'an Jiaotong University, Xi'an 710049, China

Yinuo Zhang − Center for Spintronics and Quantum Systems, State Key Laboratory for Mechanical Behavior of Materials, Xi'an Jiaotong University, Xi'an 710049, China

Yunan Lin − Center for Spintronics and Quantum Systems, State Key Laboratory for Mechanical Behavior of Materials, Xi'an Jiaotong University, Xi'an 710049, China

Yao Feng − Center for Spintronics and Quantum Systems, State Key Laboratory for Mechanical Behavior of Materials, Xi'an Jiaotong University, Xi'an 710049, China

Yongqi Hu − Center for Spintronics and Quantum Systems, State Key Laboratory for Mechanical Behavior of Materials, Xi'an Jiaotong University, Xi'an 710049, China

Muhammad Shafa − Center for Spintronics and Quantum Systems, State Key Laboratory for Mechanical Behavior of Materials, Xi'an Jiaotong University, Xi'an 710049, China

Complete contact information is available at:
https://pubs.acs.org/10.1021/acsami.3c05902

Author Contributions

Y.P. conceived and supervised the experiments. J.M. synthesized samples, and performed the measurements with the help of Y.N.Z., Y.L., Y.H., Y.F., and M.S. Y.Q.Z. fabricated the devices. Y.P. and J.M. wrote the manuscript with the input of all authors.

Notes

The authors declare no competing financial interest.

ACKNOWLEDGMENTS

REFERENCES

(1) Mueller, T.; Xia, F.; Avouris, P. Graphene Photodetectors for High-speed Optical Communications. *Nat. Photonics* **2010**, *4*, 297−301.

(2) Cai, X.; Sushkov, A. B.; Suess, R. J.; Jadidi, M. M.; Jenkins, G. S.; Nyakiti, L. O.; Myers-Ward, R. L.; Li, S.; Yan, J.; Gaskill, D. K.; Murphy, T. E.; Drew, H. D.; Fuhrer, M. S. Sensitive Room-temperature Terahertz Detection via the Photothermoelectric Effect in Graphene. *Nat. Nanotechnol.* **2014**, *9*, 814−819.

(3) Qiao, H.; Huang, Z.; Ren, X.; Liu, S.; Zhang, Y.; Qi, X.; Zhang, H. Self-Powered Photodetectors Based on 2D Materials. *Adv. Opt. Mater.* **2020**, *8*, No. 1900765.

(4) Liu, J.; Xia, F.; Xiao, D.; García de Abajo, F. J.; Sun, D. Semimetals for High-Performance Photodetection. *Nat. Mater.* **2020**, *19*, 830−837.

(5) Wei, T.; Wang, X.; Yang, Q.; He, Z.; Yu, P.; Xie, Z.; Chen, H.; Li, S.; Wu, S. Mid-Infrared Photodetection of Type-II Dirac Semimetal 1T-PtTe₂ Grown by Molecular Beam Epitaxy. *ACS Appl. Mater. Interfaces* **2021**, *13*, 22757−22764.

(6) Deng, Y.; Zhao, X.; Zhu, C.; Li, P.; Duan, R.; Liu, G.; Liu, Z. MoTe$_2$: Semiconductor or Semimetal? *ACS Nano* **2021**, *15*, 12465−12474.

(7) Dawson, W. G.; Bullett, D. W. Electronic Structure and Crystallography of MoTe$_2$ and WTe$_2$. *J. Phys. C: Solid State Phys.* **1987**, *20*, 6159−6174.

(8) Park, J. C.; Yun, S. J.; Kim, H.; Park, J.-H.; Chae, S. H.; An, S.-J.; Kim, J.-G.; Kim, S. M.; Kim, K. K.; Lee, Y. H. Phase-Engineered Synthesis of Centimeter-Scale 1T'- and 2H-Molybdenum Ditelluride Thin Films. *ACS Nano* **2015**, *9*, 6548−6554.

(9) Cho, S.; Kim, S.; Kim, J. H.; Zhao, J.; Seok, J.; Keum, D. H.; Baik, J.; Choe, D.-H.; Chang, K. J.; Suenaga, K.; Kim, S. W.; Lee, Y. H.; Yang, H. Phase Patterning for Ohmic Homojunction Contact in MoTe$_2$. *Science* **2015**, *349*, 625−628.

(10) Xu, X.; Pan, Y.; Liu, S.; Han, B.; Gu, P.; Li, S.; Xu, W.; Peng, Y.; Han, Z.; Chen, J.; Gao, P.; Ye, Y. Seeded 2D Epitaxy of Large-areaSingle-crystal Films of the Van Der Waals Semiconductor 2H MoTe$_2$. *Science* **2021**, *372*, 195−200.

(11) Xu, X.; Chen, S.; Liu, S.; Cheng, X.; Xu, W.; Li, P.; Wan, Y.; Yang, S.; Gong, W.; Yuan, K.; Gao, P.; Ye, Y.; Dai, L. Millimeter-Scale Single-Crystalline Semiconducting MoTe$_2$ via Solid-to-Solid Phase Transformation. *J. Am. Chem. Soc.* **2019**, *141*, 2128−2134.

(12) Ma, L.; Zhu, J.; Li, W.; Huang, R.; Wang, X.; Guo, J.; Choi, J. H.; Lou, Y.; Wang, D.; Zou, G. Immobilized Precursor Particle Driven Growth of Centimeter-Sized MoTe$_2$ Monolayer. *J. Am. Chem. Soc.* **2021**, *143*, 13314−13324.

(13) Kim, T.; Park, H.; Joung, D.; Kim, D.; Lee, R.; Shin, C. H.; Diware, M.; Chegal, W.; Jeong, S. H.; Shin, J. C.; Park, J.; Kang, S.-W. Wafer-Scale Epitaxial 1T', 1T'-, 2H Mixed, and 2H Phases MoTe$_2$ Thin Films Grown by Metal-Organic Chemical Vapor Deposition. *Adv. Mater. Interfaces* **2018**, *5*, No. 1800439.

(14) Xu, X.; Li, X.; Liu, K.; Li, J.; Feng, Q.; Zhou, L.; Cui, F.; Liang, X.; Lei, Z.; Liu, Z.; Xu, H. Thermodynamics and Kinetics Synergetic Phase-Engineering of Chemical Vapor Deposition Grown Single Crystal MoTe$_2$ Nanosheets. *Cryst. Growth Des.* **2018**, *18*, 2844−2850.

(15) Wang, Q.; Zheng, J.; He, Y.; Cao, J.; Liu, X.; Wang, M.; Ma, J.; Lai, J.; Lu, H.; Jia, S.; Yan, D.; Shi, Y.; Duan, J.; Han, J.; Xiao, W.; Chen, J. H.; Sun, K.; Yao, Y.; Sun, D. Robust Edge Photocurrent Response on layered type II Weyl Semimetal WTe$_2$. *Nat. Commun.* **2019**, *10*, 5736.

(16) Lai, J.; Liu, X.; Ma, J.; Wang, Q.; Zhang, K.; Ren, X.; Liu, Y.; Gu, Q.; Zhuo, X.; Lu, W.; Wu, Y.; Li, Y.; Feng, J.; Zhou, S.; Chen, J. H.; Sun, D. Anisotropic Broadband Photoresponse of Layered Type-II Weyl Semimetal MoTe$_2$. *Adv. Mater.* **2018**, *30*, No. e1707152.

(17) Sun, Y.; Xiong, J.; Wu, X.; Gao, W.; Huo, N.; Li, J. Highly Sensitive Infrared Polarized Photodetector Enabled by Out-of-plane PSN Architecture Composing of p-MoTe2, semimetal-MoTe$_2$ and n-SnSe$_2$. *Nano Res.* **2021**, *15*, 5384−5391.

(18) Singh, M. P.; Kiemle, J.; Ozdemir, I.; Zimmermann, P.; Taniguchi, T.; Watanabe, K.; Burghard, M.; Üzengi Aktürk, O.; Kastl, C.; Holleitner, A. W. Impact of Domain Disorder on Dptoelec-tronicProperties of Layered Semimetal MoTe$_2$. *2D Mater.* **2022**, *9*, 011002−011008.

(19) Wang, Q.; Li, C. Z.; Ge, S.; Li, J. G.; Lu, W.; Lai, J.; Liu, X.; Ma, J.; Yu, D. P.; Liao, Z. M.; Sun, D. Ultrafast Broadband Photodetectors Based on Three-Dimensional Dirac Semimetal Cd$_3$As$_2$. *Nano Lett.* **2017**, *17*, 834−841.

(20) Wang, J.; Luo, X.; Li, S.; Verzhbitskiy, I.; Zhao, W.; Wang, S.; Quek, S. Y.; Eda, G. Determination of Crystal Axes in Semimetallic 1T'-MoTe$_2$ by Polarized Raman Spectroscopy. *Adv. Funct. Mater.* **2017**, *27*, No. 1604799.

(21) Hoang, A. T.; Shinde, S. M.; Katiyar, A. K.; Dhakal, K. P.; Chen, X.; Kim, H.; Lee, S. W.; Lee, Z.; Ahn, J. H. Orientation-dependent Optical Characterization of Atomically Thin Transition Metal Ditellurides. *Nanoscale* **2018**, *10*, 21978−21984.

(22) Wang, X.; Shang, J.; Zhu, M.; Zhou, X.; Hao, R.; Sun, L.; Xu, H.; Zheng, J.; Lei, X.; Li, C.; Kou, L.; Feng, Q. Controlled Growth of Large-scale Uniform 1T' MoTe$_2$ Crystals with Tunable Thickness and Their Photodetector Applications. *Nanoscale Horiz.* **2020**, *5*, 954−959.

(23) Pace, S.; Martini, L.; Convertino, D.; Keum, D. H.; Forti, S.; Pezzini, S.; Fabbri, F.; Miseikis, V.; Coletti, C. Synthesis of Large-Scale Monolayer 1T'-MoTe$_2$ and Its Stabilization via Scalable hBN Encapsulation. *ACS Nano* **2021**, *15*, 4213−4225.

(24) Tsen, A. W.; Brown, L.; Levendorf, M. P.; Ghahari, F.; Huang, P. Y.; Havener, R. W.; Ruiz-Vargas, C. S.; Muller, D. A.; Kim, P.; Park, J. Tailoring Electrical Transport Across Grain Boundaries in Polycrystalline Graphene. *Science* **2012**, *336*, 1143−1146.

(25) Park, S.; Shehzad, M. A.; Khan, M. F.; Nazir, G.; Eom, J.; Noh, H.; Seo, Y. Effect of Grain Boundaries on Electrical Properties of Polycrystalline Graphene. *Carbon* **2017**, *112*, 142−148.

(26) Lanzillo, N. A.; Simbeck, A. J.; Nayak, S. K. Strain Engineering the Work Function in Monolayer Metal Dichalcogenides. *J. Phys.: Condens. Matter* **2015**, *27*, No. 175501.

(27) Liu, Y.; Guo, J.; Zhu, E.; Liao, L.; Lee, S. J.; Ding, M.; Shakir, I.; Gambin, V.; Huang, Y.; Duan, X. Approaching the Schottky-Mott Limit in van der Waals Metal-Semiconductor Junctions. *Nature* **2018**, *557*, 696−700.

(28) Wu, G.; Chung, H. S.; Bae, T. S.; Cho, J.; Lee, K. C.; Cheng, H. H.; Coileain, C. O.; Hung, K. M.; Chang, C. R.; Wu, H. C. Efficient Suppression of Charge Recombination in Self-Powered Photo-detectors with Band-Aligned Transferred van der Waals Metal Electrodes. *ACS Appl. Mater. Interfaces* **2021**, *13*, 61799−61808.

(29) Koshino, M.; Hizbullah, I. F. Magnetic Susceptibility in Three-Dimensional Nodal Semimetals. *Phys. Rev. B* **2016**, *93*, 045201−045212.

(30) Yao, J.; Yang, G. 2D Material Broadband Photodetectors. *Nanoscale* **2020**, *12*, 454−476.

(31) Zhao, S.; Dong, B.; Wang, H.; Wang, H.; Zhang, Y.; Han, Z. V.; Zhang, H. In-plane Anisotropic Electronics Based on Low-symmetry 2D materials: Progress and Prospects. *Nanoscale Adv.* **2020**, *2*, 109−139.

(32) Afzal, A. M.; Iqbal, M. Z.; Dastgeer, G.; Ahmad, A. U.; Park, B. Highly Sensitive, Ultrafast, and Broadband Photo-Detecting Field-Effect Transistor with Transition-Metal Dichalcogenide van der Waals Heterostructures of MoTe$_2$ and PdSe$_2$. *Adv. Sci.* **2021**, *8*, No. e2003713.

(33) Meng, X.-C.; Tian, H.; An, X.; Yuan, S.; Fan, C.; Wang, M.-J.; Zheng, H.-X. Field Effect Transistor Photodetector Based on Two Dimensional SnSe$_2$. *Acta Phys. Sin.* **2020**, *69*, 137801−137808.

(34) Chen, W.; Liang, R.; Wang, J.; Zhang, S.; Xu, J. Enhanced Photoresponsivity and Hole Mobility of MoTe$_2$ Phototransistors by Using an Al$_2$O$_3$ High-κ gate Dielectric. *Sci. Bull.* **2018**, *63*, 997−1005.

(35) Guo, Y.; Kang, L.; Song, P.; Zeng, Q.; Tang, B.; Yang, J.; Wu, Y.; Tian, D.; Xu, M.; Zhao, W.; Qi, X.; Zhang, Z.; Liu, Z. MoO$_3$−MoS$_2$ Vertical Heterostructures Synthesized via one-step CVD Process For Optoelectronics. *2D Mater.* **2021**, *8*, 035036−035047.

(36) Octon, T. J.; Nagareddy, V. K.; Russo, S.; Craciun, M. F.; Wright, C. D. Fast High-Responsivity Few-Layer MoTe$_2$ Photo-detectors. *Adv. Opt. Mater.* **2016**, *4*, 1750−1754.

(37) Park, J. W.; Jung, Y. S.; Park, S. H.; Choi, H. J.; Cho, Y. S. High-Performance Photoresponse in Ferroelectric d1T-MoTe$_2$-Based Vertical Photodetectors. *Adv. Opt. Mater.* **2022**, *10*, 2200898−2200907.

(38) Qiao, J.; Feng, F.; Cao, G.; Wei, S.; Song, S.; Wang, T.; Yuan, X.; Somekh, M. G. Ultrasensitive Near-Infrared MoTe$_2$ Photo-detectors with Monolithically Integrated Fresnel Zone Plate Metalens. *Adv. Opt. Mater.* **2022**, *10*, 2200375−2200383.

(39) Zhu, M.; Zhao, Y.; Feng, Q.; Lu, H.; Zhang, S.; Zhang, N.; Ma, C.; Li, J.; Zheng, J.; Zhang, J.; Xu, H.; Zhai, T.; Zhao, J. Linear Dichroism and Nondestructive Crystalline Identification of Aniso-tropic Semimetal Few-Layer MoTe$_2$. *Small* **2019**, *15*, No. e1903159.

(40) Huang, H.; Wang, J.; Hu, W.; Liao, L.; Wang, P.; Wang, X.; Gong, F.; Chen, Y.; Wu, G.; Luo, W.; Shen, H.; Lin, T.; Sun, J.; Meng, X.; Chen, X.; Chu, J. Highly Sensitive Visible to Infrared MoTe$_2$ Photodetectors Enhanced by the Photogating Effect. *Nanotechnology* **2016**, *27*, No. 445201.

(41) Chen, W.; Liang, R.; Zhang, S.; Liu, Y.; Cheng, W.; Sun, C.; Xu, J. Ultrahigh Sensitive Near-infrared Photodetectors Based on MoTe$_2$/Germanium Heterostructure. *Nano Res.* **2020**, *13*, 127−132.

(42) Wu, D.; Guo, C.; Zeng, L.; Ren, X.; Shi, Z.; Wen, L.; Chen, Q.; Zhang, M.; Li, X. J.; Shan, C. X.; Jie, J. Phase-controlled van der Waals Growth of Wafer-scale 2D MoTe$_2$ layers for Integrated High-sensitivity Broadband Infrared Photodetection. *Light Sci. Appl.* **2023**, *12*, 5.

📖 Recommended by ACS